Linear Theory and Experiments for Laminar Bias Flow Impedance: Orifice Shape Effect

L. Hirschberg*
Imperial College London, London SW7 1AY, UK

J. Guzman-Iñigo †
Imperial College London, London SW7 1AY, UK

A. Aulitto‡
Eindhoven University of Technology, 5600 MB Eindhoven, Netherlands

J. Sierra§
IMFT, 31400 Toulouse, France & UNISA, Fisciano, Italy

D. Fabre¶
IMFT, 31400 Toulouse, France

A. Morgans‖
Imperial College London, London SW7 1AY, UK

A. Hirschberg**
Eindhoven University of Technology, 5600 MB Eindhoven, Netherlands

Axisymmetric orifices with neck diameter equal to the plate thickness have been investigated. The influence of orifice geometry on the transfer impedance in presence of bias flow was predicted for laminar-flow conditions by means of a compressible Linearized-Navier-Stokes-Equations model. The results are compared to those for an incompressible-flow model and to measurements of the transfer impedance. The effect of confinement on the transfer impedance appears to be negligible for the resistance. The effect of confinement on the inertance (or reactance) can be estimated by means of Fok's classical result for thin orifices. The experimental results agree qualitatively with the predicted impedances. The Strouhal numbers for minima of the resistance are slightly higher than predicted. Negative minima indicating a whistling potentiality correspond to hydrodynamic modes of the orifice. The predicted inertance is at higher Strouhal numbers significantly larger than the measured one. The results indicate how whistling potentiality of a certain hydrodynamic mode can be promoted. The amplitude of the acoustical forcing was varied permitting to delimit the conditions under which the orifice response is linear. As the acoustic velocity amplitude approaches the steady flow velocity, the whistling potentiality of the orifices disappears.

Nomenclature

---

*Research Associate, Imperial College London, Department of Mechanical Engineering, South Kensington Campus, London SW7 2AZ, UK, AIAA Member.

†Research Associate, Imperial College London, Department of Mechanical Engineering, South Kensington Campus, London SW7 2AZ, UK.

‡PhD student, Department of Mechanical Engineering, Eindhoven University of Technology, P.O. Box 513, 5600 MB Eindhoven, Netherlands.

§PhD Student, Institut de Mécanique des Fluides de Toulouse, IMFT, Université de Toulouse, CNRS; Allée Camille Soula, 31400 Toulouse, France & DIIN, Universitá degli Studi di Salerno, Via Giovanni Paolo II, 84084 Fisciano (SA), Italy.

¶Lecturer, Institut de Mécanique des Fluides de Toulouse, IMFT, Université de Toulouse, CNRS; Allée Camille Soula, 31400 Toulouse, France.

‖Professor of Thermofluids, Imperial College London, Department of Mechanical Engineering, South Kensington Campus, London SW7 2AZ, UK.

**Professor emeritus, Department of Applied Physics, Fluids and Flows, Eindhoven University of Technology, P.O. Box 513, 5600 MB Eindhoven, Netherlands

c = Sound speed, $\mathrm{m \cdot s^{-1}}$
He = Helmholtz number
i = imaginary unit, $\mathrm{i}^2 \equiv -1$
$\mathrm{Im}\{\dots\}$ = Imaginary part
L = Length, m
M = Mach number
p = Pressure, Pa
q = Unsteady volumetric flow, $\mathrm{m^3 \cdot s^{-1}}$
Q = Steady volumetric flow, $\mathrm{m^3 \cdot s^{-1}}$
r = reflection coefficient
R = Radius, m
Re = Reynolds number
$\mathrm{Re}\{\dots\}$ = real part
$\mathbf{u}$ = velocity, $\mathrm{m \cdot s^{-1}}$
u = axial velocity component, $\mathrm{m \cdot s^{-1}}$
U = Speed, $\mathrm{m \cdot s^{-1}}$
Z = Impedance, $\mathrm{m \cdot s^{-1}}$
α = Factor
δ = thickness, m
Δ = Difference
θ = Angle, rad
ν = Kinematic viscosity of air, $1.5 \times 10^{-5} \mathrm{m^2 s^{-1}}$
ρ = Density, $\mathrm{kg \cdot m^{-3}}$
∇ = Gradient operator, $\mathrm{m^{-1}}$
Φ = porosity
ω = Angular frequency, $\mathrm{rad \cdot s^{-1}}$

Subscripts

0 = Steady value
1 = Displacement
2 = Momentum
cal = Calibration
cor = Correction
dif = Diffuser
dst = Downstream
frc = Forcing
hfl = High-frequency limit
I = Imaginary part
inl = Inlet
max = Maximum
mic = Microphone
min = Minimum
msr = Measurement
lfl = Low-frequency limit
o = Open
orf = Orifice
oul = Outlet
r = Radial component
R = Real part
s = Sample
set = User set

tws = Thwaites
ust = Upstream
x = Axial component

Superscript

$'$ = Indicates fluctuation
$\bar{}$ = Dimensionless quantity

I. Introduction

In many real-world applications—including aeroengines and power gas turbine combustors —one encounters a flow passing through orifices in plates [1–5]. Under unfavorable conditions these orifices produce sound; i.e., they whistle.

Whistling of sharp edged circular orifices in finite-thickness plates was first experimentally observed by Sondhauss [6] and reported by Rayleigh [7]. Experimental investigations by Anderson [8–12] and later by Jing and Sun [13], Karthik et al. [14], Testud et al. [15], Lacombe et al. [16], Zhou and Bodén [17], Su et al. [18], Moers et al. [19] and Wu et al. [20] provided more insight into the controlling parameters. Nair and Sujith [21] studied the chaotic behavior around the onset of whistling. Lacombe et al. [16], Moussou [22] and Fabre et al. [4] used the Nyquist criterion [23] to obtain a prediction of the sharp-edged orifice's whistling based on its acoustic transfer impedance. Jing and Sun [13] used a discrete-vortex model to predict the acoustical response of orifices. Ji and Zhao [24] used a Lattice Boltzmann model to predict the acoustic impedance of orifices. Su et al. [18] and Chen et al. [25] used Unsteady Reynolds Averaged Navier Stokes (URANS) simulations to predict the transfer impedance of thick sharp edged orifices. Alenius et al. [26, 27] and Sorvadi et al. [28] used compressible Large Eddy Simulations (LES) to study sound production by a sharp-edged thick-plate orifice. Kiergegaard et al. [29, 30] and later Fabre et al. [4] used Linearized Navier Stokes Equation (LNSE) models to study the whistling conditions of an orifice in a thick plate.

In particular, Fabre et al. [3] reported a numerical simulation based study of acoustic response of a single sharp-edged circular-shaped perforation in an infinitely-thin plate. In a subsequent publication—Fabre et al. [4] reported a numerical simulation based investigation of whistling by a single sharp-edged cylindrical perforation in a plate of finite thickness. In both studies a laminar steady base flow was established in the direction of the perforation's axis of rotational symmetry. The laminar base flow was then used as the initial condition, for simulations employing a Linearized Navier-Stokes Equations (LNSE) code. These LNSE simulations consisted of acoustically perturbing the base flow at a fixed frequency. The acoustic impedance of the circular perforation was determined for the set frequency. This was repeated for an ensemble of frequencies.

We note that for bias flow through slit-shaped orifices, the influence of the geometry of the edges was investigated experimentally by Tonon et al. [31] and Moers et al. [19]. Moreover, in the absence of flow the influence of a cylindrical orifice's shape on its transfer impedance was investigated by Temiz et al. [32]. The focus of investigation of the presently reported study was on cylindrical orifices of various shapes subject to bias flow.

A sharp-edged orifice subject to a bias flow and upstream acoustic forcing, displays local minima in the real part of the transfer impedance. If, this local minimum is negative it is said that there is whistling potentiality. The Strouhal numbers at which these minima occur correspond to the convection time close to an integer number of shear perturbations from the orifice's inlet to its outlet. The first local minimum corresponds to the presence within the orifice of one perturbation, the second to two, etc. Ergo, in this text these local minima of the real part of the transfer impedance will be referred to as the first, second, etc. hydrodynamic modes.

Guzman-Iñigo et al. [5], made a first step to investigate —by means of numerical simulations and the use of an semi-analytical model (based on Howe's analogy [33])—the influence of the shape of a single circular perforation in a plate of finite thickness. Indeed, Guzman-Iñigo et al. [5] reported results for a slightly rounded upstream inlet of the perforation. They reported that very small changes of the perforation's inlet edge can bring about significant modifications in its acoustic response. One notes that Guzman-Iñigo et al. [5] state: "…this paper is restricted to small modifications of the edge when compared with the radius of the hole." Indeed, in Ref. [5] the influence of more significant rounding of the inlet edge was left to the future.

We note that sound production by orifices—in the situation as sketched above—is similar to that in: whistler nozzles, horns, diffusers and shalow cavities [34–36]. A qualitative explanation of this sound production mechanism—in terms of Howe's analogy [33]—was provided by Hirschberg et al. [34].

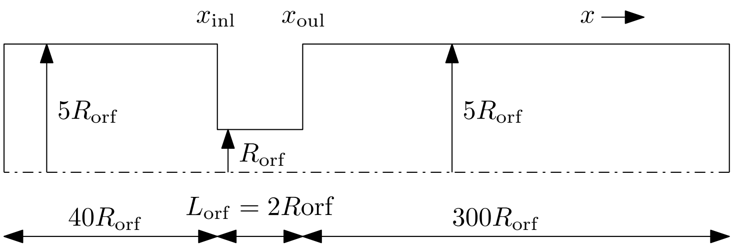

Fig. 1 Sketch of the computational domain.

The present work builds on Fabre's et al. [3, 4] & Guzman-Iñigo's et al. [5] work. Indeed, we used a LNSE-simulation approach to investigate the transfer impedance of an orifice in a plate of finite thickness—in the presence of laminar flow through it. In addition, original complementary measurements were carried out using an impedance tube for the four investigated orifice shapes, to wit: a sharp-edged orifice, a rounded-inlet and sharp-outlet orifice, a sharp-inlet and rounded-outlet orifice, a convergent-divergent nozzle orifice (i.e., with a rounded inlet followed by a diffuser section).

We report theoretical results on the influence of significant rounding of the inlet edge. In addition, we present—hitherto unreported—results of a systematic investigation of the effect of a rounded downstream edge. We also numerically and experimentally investigated the acoustic response of a convergent-divergent-nozzle orifice. Moreover, the experiments were used to investigate the influence of the upstream acoustic-forcing amplitude on the results. This was done to probe the limits of the LNSE model's application regime. In the experiments the orifice is confined within a tube. The influence of this confinement is quantified for the sharp edged orifice.

The compressible numerical-simulation approach—including a description of the computational domain, the equations which are solved and boundary conditions—used to preform the investigation are succinctly described in §II and §II.B.2. In §III, the experimental approach is described. Results are reported in §IV. Two distinct LNSE codes—viz. incompressible and compressible LNSE—are compared in §IV.A. Results of the parameter study performed with the compressible LNSE code are provided in §IV.B. Complementary experimental results are provided and compared to numerical simulation results in §IV.C. Conclusions are drawn in §VI.

II. The numerical simulation approach

In §II.A, a description of the numerical domain is provided. The equations solved for the numerical simulation (mean flow and compressible LNSE) are provided in §II.B. The reader is referred to Guzman-Iñigo et al. [37] for a more expansive discussion of the compressible LNSE model. The boundary conditions used are discussed in §II.C. A description of how the impedance is determined is provided in §II.D.

A. The computational domain

In Fig. 1, a sketch of the computational domain used for the presently-reported investigation is shown. The dashed dotted line is a cylindrical-symmetry axis. The cylindrical symmetric domain had a radius of $5R_{\text{orf}}$ to the left (upstream) and right (downstream) of a constriction with a minimum radius R_{orf}. The length of this constriction

$$L_{\text{orf}} = 2R_{\text{orf}} \tag{1}$$

was fixed for all presently-reported numerical investigations. The lengths of the parts of the domain upstream and downstream from the constriction—henceforth referred to as the orifice—were $40R_{\text{orf}}$ and $300R_{\text{orf}}$, respectively. The axial position of the in- and outlet are—in Fig. 1—indicated with x_{inl} and x_{oul}.

The four orifice shapes considered for our numerical investigation—shown in Fig. 2—were:

(a) a sharp-edged circular orifice (Fig. 2(a)),
(b) a rounded upstream edge with a sharp-edged outlet (Fig. 2(b)),
(c) a sharp-edged inlet with a rounded outlet (Fig. 2(c)),
(d) a convergent-divergent nozzle geometry (Fig. 2(d)).

The rounded-inlet orifice (Fig. 2(b) had an upstream-edge radius of curvature, R_{ust}. The rounded-outlet orifice (Fig. 2(c)) had an downstream-edge radius of curvature, R_{dst}. The convergent-divergent nozzle the diffuser angle of the convergent-divergent nozzle orifice (Fig. 2(d)) was

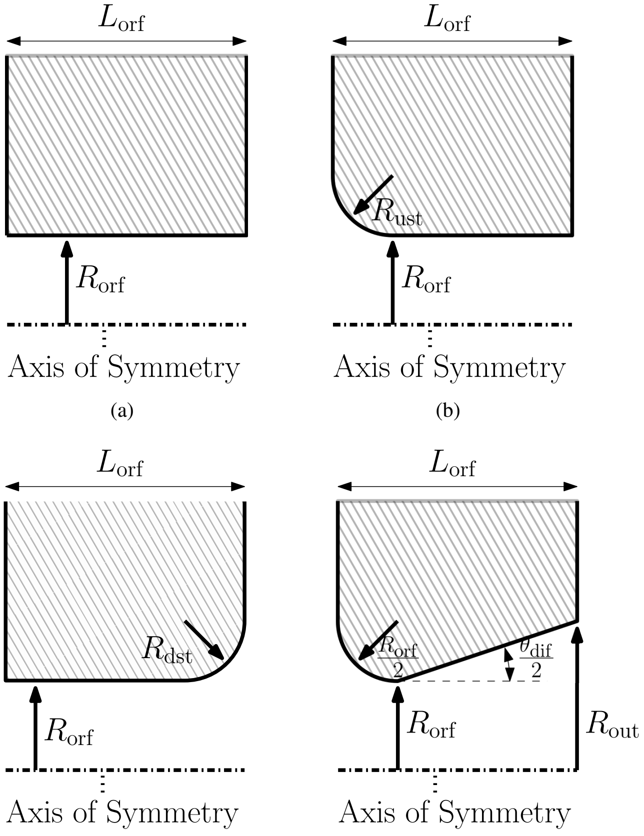

(a) (b)

(c) (d)

Fig. 2 Orifice shapes considered for the numerical simulation study: (a) sharp-edged orifice (b) rounded upstream edge (c) rounded downstream edge (d) convergent-divergent nozzle.

$$\theta_{\text{dif}} = 2\arctan\left(\frac{R_{\text{out}} - R_{\text{orf}}}{L_{\text{orf}} - (R_{\text{orf}}/2)}\right) \tag{2}$$

where the neck-cross-section radius R_{orf} and plate thickness L_{orf} were fixed (Eq. (1)) and the radius of the outlet cross section R_{out} (defined in Fig. 2(d)) was varied systematically.

B. The solved equations

The equations solved to establish the mean flow are described in §II.B.1. In §II.B.2 the linearized Navier-Stokes equations (LNSE) are presented.

1. Mean flow

The dimensionless steady incompressible-flow equations (mass and momentum conservation)—which are solved to establish a mean flow—are:

$$\bar{\nabla}\cdot\bar{\mathbf{u}} = 0 \tag{3}$$

$$\bar{\mathbf{u}}\cdot\bar{\nabla}\bar{\mathbf{u}} = -\frac{1}{\bar{\rho}}\bar{\nabla}\bar{p} + \frac{1}{Re_{\text{orf}}}\bar{\nabla}^2\bar{\mathbf{u}} \tag{4}$$

where

$$Re_{\text{orf}} \equiv \frac{2R_{\text{orf}}U_{\text{orf}}}{\nu} \tag{5}$$

is the Reynolds number based on the orifice diameter $2R_{\text{orf}}$ and U_{orf} the averaged axial flow speed at the orifice's inlet. U_{orf} is defined as follows:

$$U_{\text{orf}} = \frac{Q_{\text{orf}}}{\pi R_{\text{orf}}^2} \tag{6}$$

where Q_{orf} is the volumetric flow rate through the orifice.

These dimensionless equations were discretised using the finite-element method within the FEniCSx computing platform [38] and a first-order accurate Newton integration scheme. A basis of Arnold-Brezzi-Fortin MINI-elements [39], with P_1 elements for the pressure and P_{1b} elements for each velocity component. The discrete non-linear problem was solved using the Newton method.

2. Linearized Navier-Stokes equations

The dimensionless compressible linearized Navier-Stokes equations (LNSE) are:

$$He_{\text{orf}}\frac{\partial\bar{\rho}'}{\partial\bar{t}} = -\bar{\rho}_0\bar{\nabla}\cdot(\bar{\mathbf{u}}') - \bar{\mathbf{u}}_{\mathbf{0}}\cdot\bar{\nabla}\bar{\rho}' \tag{7}$$

$$He_{\text{orf}}\frac{\partial\bar{\mathbf{u}}'}{\partial\bar{t}} + \bar{\nabla}\cdot(\bar{\mathbf{u}}'\bar{\mathbf{u}}_{\mathbf{0}} + \bar{\mathbf{u}}_{\mathbf{0}}\bar{\mathbf{u}}' + \bar{\rho}'\bar{\mathbf{u}}_{\mathbf{0}}\bar{\mathbf{u}}_{\mathbf{0}}) = -\bar{\nabla}\bar{p} + \frac{M_{\text{orf}}}{Re_{\text{orf}}}\bar{\nabla}^2\bar{\mathbf{u}} \tag{8}$$

where

$$He_{\text{orf}} = \frac{2R_{\text{orf}}\omega}{c_{\text{orf}}} \tag{9}$$

is a Helmholtz number based on the—upstream boundary imposed—forcing frequency, ω, the orifice's diameter, $2R_{\text{orf}}$, and the sound speed, c_{orf} at its inlet; and

$$M_{\text{orf}} = \frac{U_{\text{orf}}}{c_{\text{orf}}} \tag{10}$$

is the Mach number at the orifice's inlet.

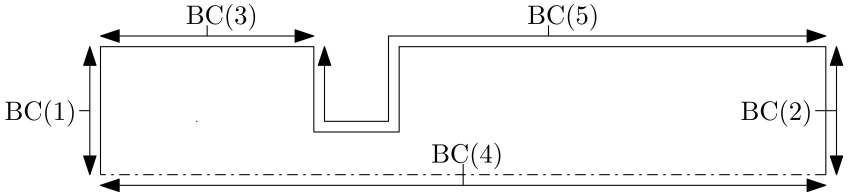

Fig. 3 Sketch of where the boundary conditions (BCs) are applied.

These LNSE simulations—using the previously computed mean flow as a background flow—were performed using the FEniCSx computing platform [38] and a second-order accurate finite-element method. N.b., these equations were solved in the frequency domain.

A detailed description of the numerical model for the incompressible flow simulations are found in Fabre et al. [4].

C. Boundary conditions

In Fig. 3, a sketch of where the boundary conditions (BCs) are applied is shown. The pipe segments, when present upstream or downstream of the orifice have a cross sectional radius of $5R_{\text{orf}}$. Two different sets of boundary conditions are applied to establish the mean flow and to perform the LNSE simulations. These boundary conditions are briefly described in §II.C.1 and §II.C.2, respectively.

1. Mean-flow boundary conditions

The boundary conditions applied to establish the mean flow were:

BC(1): $u_x = U_{\text{orf}} {R_{\text{orf}}}^2/(5R_{\text{orf}})^2$
BC(3): $u_r = 0$
BC(4): $u_r = 0$
BC(5): $u_x = 0$ and $u_r = 0$

where BC(1) is an inflow boundary condition, BC(3) a slip boundary condition, BC(4) is a symmetry boundary condition and BC(5) is a no-slip boundary condition.

2. LNSE boundary conditions

The boundary conditions used to perform the LNSE simulation were:

BC(1): non-reflective boundary condition
BC(2): non-reflective boundary condition
BC(4): $u_{r,R} = 0$ and $u_{r,I} = 0$ (symmetry boundary condition)
BC(5): $u_{x,R} = 0$ and $u_{x,I} = 0$ (no-slip boundary condition)
BC(5): $u_{r,R} = 0$ and $u_{r,I} = 0$ (no-slip boundary condition)

where BC(4) is a symmetry boundary condition and BC(5) is a no-slip boundary condition. N.b., the subscripts R and I indicate the real and imaginary components, respectively. Moreover, at BC(1) acoustic forcing at a fixed frequency ω was applied.

The boundary conditions for the incompressible flow simulation results are found in Ref. [4]. In the case of the incompressible flow model results, there was a pipe of radius $5R_{\text{orf}}$ upstream of the orifice. The downstream flow emerged into free space, bounded by the downstream side of the orifice plate.

D. Determination of the impedance

The transfer impedance, Z, of the orifice is defined as follows

$$Z = \frac{p'_{\text{ust}} - p'_{\text{dst}}}{q'} = Z_R + \mathrm{i}Z_I \tag{11}$$

where q' is the volumetric flow rate fluctuation. p'_{ust} and p'_{dst} are the up- and downstream pressure fluctuation; viz., up- and downstream of the orifice. In dimensionless form the impedance is

$$\bar{Z} = \bar{Z}_R + \mathrm{i}\bar{Z}_I = \frac{R_{\mathrm{orf}}^2}{\rho_{\mathrm{orf}} U_{\mathrm{orf}}} Z \tag{12}$$

The impedance is a function of the forcing frequency ω, which in dimensionless form becomes a Strouhal number, to wit:

$$\Omega \equiv \frac{R_{\mathrm{orf}}}{U_{\mathrm{orf}}} \omega \tag{13}$$

The up- and downstream pressure fluctuations are taken to be composed of up- and downstream traveling plane waves in the pipe segments up and downstream of the orifice $p_{\mathrm{ust}}^{\pm}$ and $p_{\mathrm{dst}}^{\pm}$, respectively. These wave amplitudes are obtained by wave decomposition of the cross-sectional averaged results of the simulations—the multi-microphone method was used for this. The acoustic field at the axial orifice inlet and outlet positions x_{inl} and x_{oul} (defined in Fig. 1)—is obtained by extrapolation, namely

$$p'_{\mathrm{ust}} = p_{\mathrm{ust}}^{+} \exp\left(-\mathrm{i}\frac{\omega}{c+u_0} x_{\mathrm{inl}}\right) + p_{\mathrm{ust}}^{-} \exp\left(\mathrm{i}\frac{\omega}{c-u_0} x_{\mathrm{inl}}\right) \tag{14}$$

$$p'_{\mathrm{dst}} = p_{\mathrm{dst}}^{+} \exp\left(-\mathrm{i}\frac{\omega}{c+u_0} x_{\mathrm{oul}}\right) + p_{\mathrm{dst}}^{-} \exp\left(\mathrm{i}\frac{\omega}{c-u_0} x_{\mathrm{oul}}\right) \tag{15}$$

In terms of velocity fluctuations, one has

$$u'_{\mathrm{ust}} = \frac{p_{\mathrm{ust}}^{+}}{\rho c} \exp\left(-\mathrm{i}\frac{\omega}{c+u_0} x_{\mathrm{inl}}\right) - \frac{p_{\mathrm{ust}}^{-}}{\rho c} \exp\left(\mathrm{i}\frac{\omega}{c-u_0} x_{\mathrm{inl}}\right) \tag{16}$$

$$u'_{\mathrm{dst}} = \frac{p_{\mathrm{dst}}^{+}}{\rho c} \exp\left(-\mathrm{i}\frac{\omega}{c+u_0} x_{\mathrm{oul}}\right) - \frac{p_{\mathrm{dst}}^{-}}{\rho c} \exp\left(\mathrm{i}\frac{\omega}{c-u_0} x_{\mathrm{oul}}\right) \tag{17}$$

The unsteady volumetric flow rate fluctuation is then taken to be

$$q' = 25\pi R_{\mathrm{orf}}^2 u'_{\mathrm{ust}} \tag{18}$$

III. Experimental approach

A succinct description of the experimental setup is provided in §III.A. The experimental method used to determine the transfer impedance is briefly described in §III.C. Appendix A provides a description of the calibration of the flow controller used to set the steady bias flow.

A. Experimental setup

In Fig. 4, a sketch of the experimental setup used to determine the transfer impedance of an orifice subject to a bias flow is shown. A volume-flow rate $\dot{Q}$ is imposed— using a calibrated flow controller—on the upstream side (left-hand side of the orifice in Fig. 4) of the orifice to impose the bias flow.

The radius of the pipe upstream and downstream from the orifice was $R_{\mathrm{pipe}} = 25$ mm. The shapes of the orifices could be varied. Four of the shapes described in Fig. 2 were investigated—viz.: the sharp edge orifice, an orifice with rounded upstream edge $R_{\mathrm{ust}} = 2R_{\mathrm{orf}}$, an orifice with rounded downstream edge $R_{\mathrm{dst}} = 2R_{\mathrm{orf}}$ and a convergent divergent orifice with $R_{\mathrm{out}} = 7R_{\mathrm{orf}}/4$.

Acoustic forcing was done by means of a 25 W loudspeaker fixed flush at the upstream-pipe end. The imposed acoustic-forcing signal was harmonic and its amplitude could be varied. For a fixed forcing amplitude a preset frequency range was scanned. Six pre-polarized 1/4 inch microphones (type BWSA, sensitivity 50 $\mathrm{mV} \cdot \mathrm{Pa}^{-1}$) mounted flush upstream from the orifice under investigation were used to recorded the acoustic response due to forcing.

The samples used were very precise (accuracy of the order of 0.01 mm) reproductions of the geometries depicted in Fig. 2. E.g., the sharp-edge were manufactured such that they were literally razor sharp. This was confirmed by the fact that the transfer impedance measurement results remained identical when the position of the orifice with sharp square edged was inverted with respect to the flow direction.

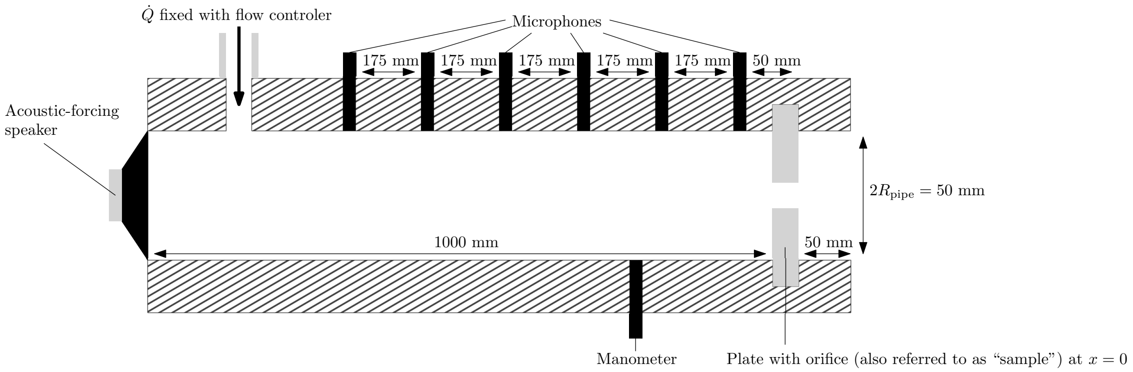

Fig. 4 Sketch of the experimental setup.

B. Acoustic-forcing amplitude

In the experiments, a forcing amplitude was applied using the upstream speaker (as sketch in Fig. 4). This was done by having the user set a forcing voltage V_{frc} target. The actual harmonic pressure fluctuation was measured by means of the calibrated microphone 50 mm upstream of downstream side of the orifice. A feedback system tuned V_{frc} to keep $|p'|$ constant as the frequency was stepwise changed.

The relative velocity-forcing amplitude can be determined, using

$$\frac{|u'_{\mathrm{frc}}|}{U_{\mathrm{orf}}} = \frac{|p'|}{\pi \rho U_{\mathrm{orf}}^2 |\bar{Z}|} \tag{19}$$

One notes that $|\bar{Z}|$ is a function of the forcing frequency (or the Strouhal number Ω). Two order-of-magnitude limits of $|u'_{\mathrm{frc}}|/U_{\mathrm{orf}}$, can be explored: the high-frequency and the low-frequency limits.

Let us start with the high-frequency limit. In this limit $\bar{Z}$ is dominated by the inertia $\bar{Z}_I$, which in turn is of the order-of-magnitude of Ω. One finds:

$$\lim_{\Omega \to \infty} \frac{|u'_{\mathrm{frc}}|}{U_{\mathrm{orf}}} = \left(\frac{|u'_{\mathrm{frc}}|}{U_{\mathrm{orf}}} \right)_{\mathrm{hfl}} \simeq \frac{1}{\pi \Omega} \frac{|p'|}{\rho U_{\mathrm{orf}}^2} \tag{20}$$

Moving to the low-frequency limit, one applies Bernoulli's quasi-steady equation ($p_{\mathrm{orf}} = \rho U_{\mathrm{orf}}^2/2$), one has

$$U_{\mathrm{orf}} \pm u'_{\mathrm{frc}} = \sqrt{\frac{2\left(p_{\mathrm{orf}} \pm p'\right)}{\rho}} \simeq U_{\mathrm{orf}} \left(1 \pm \frac{p'}{\rho U_{\mathrm{orf}}^2} \right) \tag{21}$$

one finds

$$\lim_{\Omega \to 0} \frac{|u'_{\mathrm{frc}}|}{U_{\mathrm{orf}}} = \left(\frac{|u'_{\mathrm{frc}}|}{U_{\mathrm{orf}}} \right)_{\mathrm{lfl}} \simeq \frac{|p'|}{\rho U_{\mathrm{orf}}^2} \tag{22}$$

Ergo, going forward $|\bar{p}'| = |p'|/(\rho U_{\mathrm{orf}}^2)$ will be used as an indication for the order-of-magnitude of $|u'|/U_{\mathrm{orf}}$.

C. Experimental determination of the transfer impedance

The transfer impedance was determined using the approach described in more detail by Aulitto et al. [40]. It is based on the measurement of the reflection coefficient with and without the presence of an orifice—also referred to as a "sample"—at $x = 0$. Indeed, the sample could be replaced by a ring to create a smooth open pipe. The reflection coefficient of the open pipe, r_o and the reflection coefficient with the presence of an orifice, r_s were measured using the method described in Jang and Ih [41].

The dimensionless radiation impedance of the open pipe was calculated using

$$\bar{Z}_o = \frac{1 + r_o}{1 - r_o} \tag{23}$$

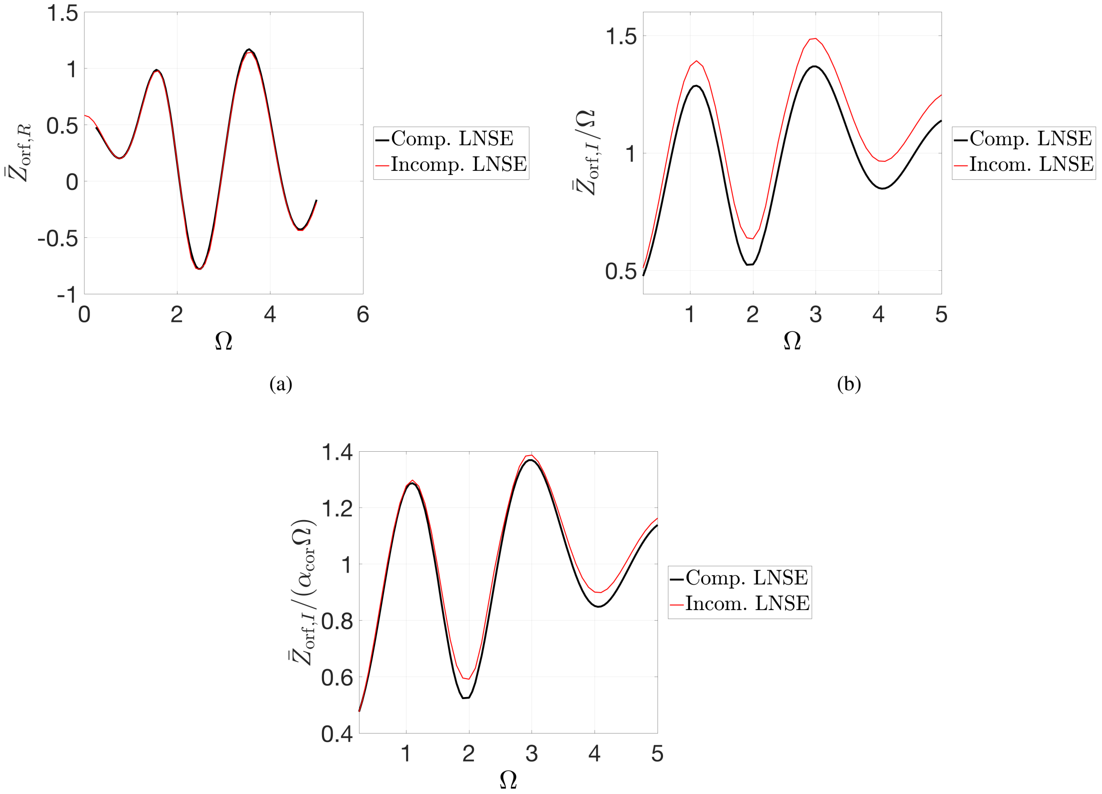

(a)

(b)

(c)

Fig. 5 Sharp-edged orifice compared compressible LNSE simulation compared to Fabre's et al. incompressible LNSE results for $Re_{\mathrm{orf}} = 1.2 \times 10^3$: (a) $\bar{Z}_R$ vs. Ω (b) $\bar{Z}_I/\Omega$ vs. Ω (c) $\bar{Z}_I/(\alpha_{\mathrm{cor}}\Omega)$ vs. Ω.

and the same expression was used to determined the impedance in the presence of a perforated plate

$$\bar{Z}_s = \frac{1 + r_s}{1 - r_s} \tag{24}$$

The transfer impedance was then determined as follows

$$\bar{Z}_{\mathrm{orf}} = \bar{Z}_o - \bar{Z}_s \tag{25}$$

IV. Results

Most of the numerical simulation results presented here, were obtained with the compressible LNSE code described in §II.B.2. However, in §IV.A results for the sharp-edged orifice case are compared to simulations obtained with an incompressible LNSE code described by Fabre et al [3, 4]. In §IV.C, LNSE results are compared to original empirical data obtained using the experimental setup and approach briefly described in §III. All results in this section were obtained with $Re_{\mathrm{orf}} = 1.2 \times 10^3$,the reported measurements were also obtained for this Reynolds number. Under these circumstances the flow within the orifice is expected to be laminar, as assumed in the theoretical model.

A. Comparison of compressible and incompressible LNSE results

In Fig. 5 results for sharp-edged orifice (Fig. 2(a)) obtained with the compressible LNSE code described in §II.B.2 are compared to results obtained with an incompressilbe LNSE code (the incompressible LNSE code was developed and used for investigations by Fabre et al. [3, 4]). One observes three minima of the real part of the impedance corresponding

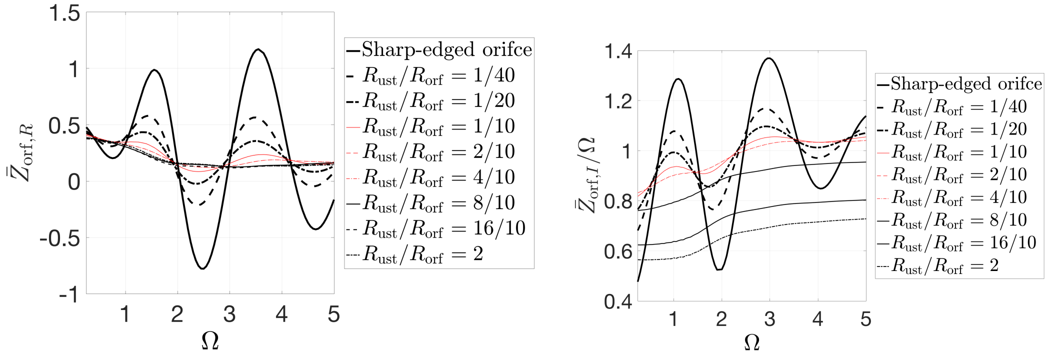

(a)

(b)

Fig. 6 Rounded-inlet orifice compared to the sharp-edged orifice compressible LNSE simulation results for $Re_{\mathrm{orf}} = 1.2 \times 10^3$: (a) $\bar{Z}_R$ vs. Ω (b) $\bar{Z}_I/\Omega$ vs. Ω.

to the first three hydrodynamic modes. The first mode (at $\Omega \simeq 0.7$) has no whistling potentiality as the minima remains positive. The second ($\Omega \simeq 2.5$) and third ($\Omega \simeq 4.7$) hydrodynamic mode have a strong whistling potentiality.

One should note that the results produced with the incompressible LNSE code were obtained with a different computational domain and boundary conditions. Indeed, for the incompressible case the boundary condition imposed at BC(5) in Fig. 3, were—excluding the plate and orifice were a no-slip condition was imposed—slip boundary conditions. Moreover, I.e., the results for the incompressible case are a model for a sharp-edged orifice in a plate between an upstream duct of radius $5R_{\mathrm{orf}}$ and a downstream unducted space.

In Fig. 5(a), one observes that the results for the real part of the transfer impedance, $\bar{Z}_R$, overlap within ca. 1%.

In Fig. 5(b) one observes a deviation of not more than 22% in, $\bar{Z}_I/\Omega$, the imaginary part of the transfer impedance divided by the Strouhal number. This deviation is due to a confinement effect on $\bar{Z}_{\mathrm{orf},I}$. Indeed, using Fok's formula [42] the incompressible LNSE result can be corrected for this confinement effect by dividing the imaginary part of the transfer impedance by a correction factor $\alpha_{\mathrm{cor}} = 1.073$. The result is shown in Fig. 5(c), one notes that there is overall much better agreement between the results of the two flow simulations. Moreover, the maximum deviation—at the first local minimum or hydrodynamics mode—is reduced to not more that 14% when applying this correction. This significant reduction indicates that the difference in $\bar{Z}_{\mathrm{orf},I}$ is mainly due to confinement effects. We concluded that for the LNSE simulations the fact that the downstream side is ducted or unducted does not play a major role.

The fact that the real part of the impedance is not affected by the confinement indicates that, the dissipation or production of sound occurs locally within the orifice or in a region close to the exit of the orifice. Indeed, the dissipation is related to the modulation of the shear layer at the flow separation point at the orifice inlet. Sound production is related to the exit of the perturbed shear layer from the orifice. The imaginary part of the impedance corresponding to the inertia of the flow is less concentrated and therefore more sensitive to confinement.

B. Parameter variation: compressible LNSE simulation results

In Fig. 6, simulation results are shown for the rounded inlet geometry (2(b)). $R_{\mathrm{ust}}/R_{\mathrm{orf}}$ was varied from 1/40 to 2. The results are compared with the sharp-edged orifice case (thickest solid black line). One observes in Fig. 6(a) that rounding the even a little bit—e.g. $R_{\mathrm{ust}}/R_{\mathrm{orf}} = 1/40$—drastically diminishes, by ca. a factor two, the whistling potentiality of the orifice. Indeed, for $R_{\mathrm{ust/R_{orf}}} > 1/20$ $Z_{\mathrm{orf},R} > 0$; i.e. the results for $R_{\mathrm{ust/R_{orf}}} > 1/20$ indicate that the whistling potentiality vanishes. This confirms and extends the results obtained by Guzman-Iñigo et al. [5].

Results, for the rounded outlet geometry (Fig. 2(c)) are shown in Fig. 7. $R_{\mathrm{dst}}/R_{\mathrm{orf}}$ was varied logarithmically from 1/10 to 2. The results are compared to the sharp-edge orifice case (thickest solid black line). One observes, in Fig. 7(a), that as $R_{\mathrm{dst}}/R_{\mathrm{orf}} > 4/10$ the first hydrodynamic mode (minimum of the real part of the transfer impedance) emerges as the only source of whistling potentiality. Indeed, $R_{\mathrm{dst}}/R_{\mathrm{orf}} > 4/10$ the second minimum in $\bar{Z}_{\mathrm{orf},R}$ vanishes.

In Fig. 8, results for the convergent-divergent nozzle orifice (Fig. 2(d)) are shown in Fig. 8. θ_{dif} was varied from 0.00 rad to 1.18 rad. One observes as expected an absence of predicted whistling potentiality for $\theta_{\mathrm{dif}} = 0$. This corresponds to the configuration in Fig. 2(b). As θ_{dif} is increased, one observes the emergence of a dominant first hydrodynamic mode (minimum in $\bar{Z}_{\mathrm{orf},R}$) (Fig. 8(a)).

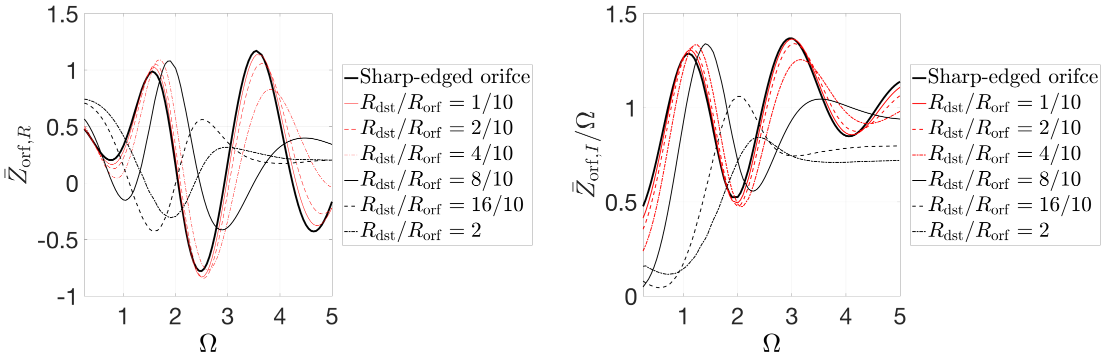

(a) (b)

Fig. 7 Rounded-outlet orifice response compared to that of the sharp-edged orifice compressible LNSE simulation results for $Re_{\mathrm{orf}} = 1.2 \times 10^3$: (a) $\bar{Z}_R$ vs. Ω (b) $\bar{Z}_I/\Omega$ vs. Ω.

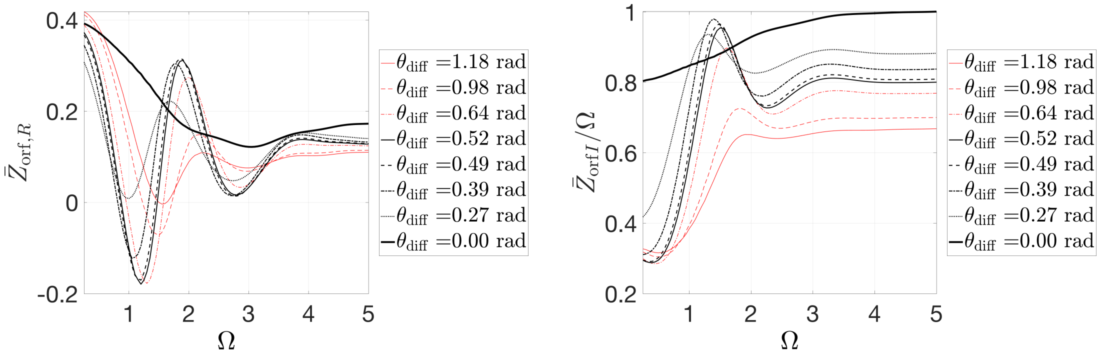

(a) (b)

Fig. 8 Transfer impedance for convergent-divergent nozzle geometry compressible LNSE simulation results for $Re_{\mathrm{orf}} = 1.2 \times 10^3$ as a function of the Strouhal numberΩ: (a) $\bar{Z}_R$ vs. Ω (b) $\bar{Z}_I/\Omega$ vs. Ω.

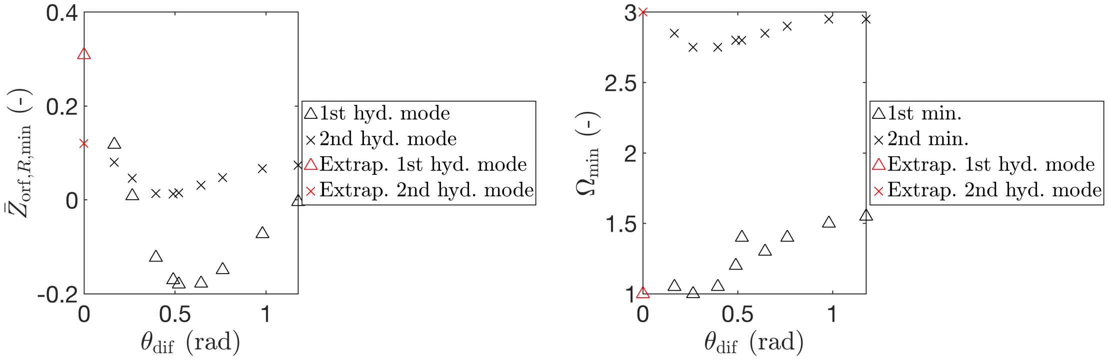

(a) (b)

Fig. 9 Convergent-divergent nozzle geometry compressible LNSE simulation hydrodynamic modes for $Re_{\mathrm{orf}} =$ 1200: (a) $\bar{Z}_{R,\mathrm{min}}$ vs. θ_{dif} (b) Ω_{min} vs. θ_{dif}

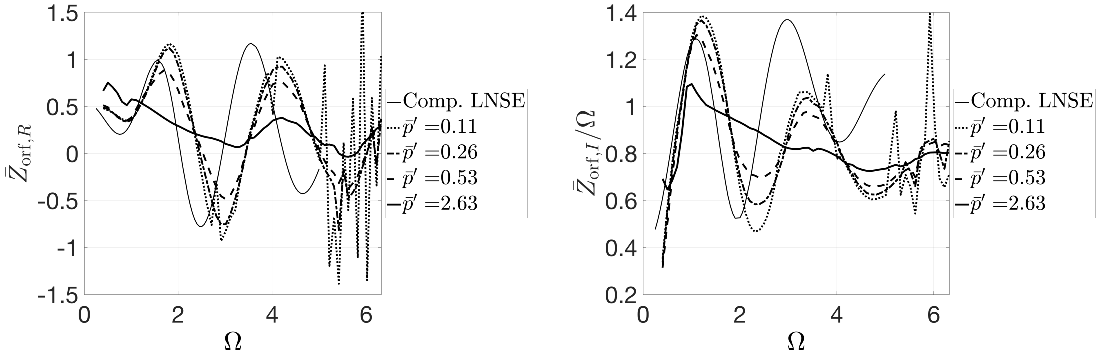

(a)

(b)

Fig. 10 Sharp-edged orifice measurements compared to compressible LNSE results: (a) $\bar{Z}_R$ vs. Ω (b) $\bar{Z}_I/\Omega$ vs. Ω.

In Fig. 9(a), the first and second minima in $\bar{Z}_{\mathrm{orf},R}$ are shown as a function of θ_{dif}. The Strouhal number at which these minima occur, Ω_{min}, are plotted as a function of θ_{dif} in Fig. 9(b). One notes that the first and second minima occur at $\Omega_{\mathrm{min}} \simeq 1.25$ and $\Omega_{\mathrm{min}} \simeq 2.9$, respectively. Moreover, one notes that the results predict an optimum in whistling potentiality of the first hydrodynamic mode for $\theta_{\mathrm{dif}} = 0.52$ rad, while the second hydrodynamic mode remains silent for the conditions investigated.

Thus, the shape of an orifice can be changed in order to optimize predicted whistling potentiality. We note that the possibility for a whistling potentiality of the third hydrodynamic mode is obtained for the sharp edged orifice at sufficiently high Reynolds numbers.

C. Comparison of numerical and experimental results

All the experimental and numerical simulation results reported here were obtained with $Re_{\mathrm{orf}} = 1.2 \times 10^3$.

In Fig. 10, experimental results obtained with the sharp-edged orifice are compared to those of the compressible LNSE model. The experimental results were obtained with four dimensionless-forcing amplitudes $\bar{p}' = 0.11$ (thick dotted line), 0.26 (thick dashed-dotted line), 0.53 (thick dashed line) and 2.63 (thick solid line). One notes that the signal is affected by noise for $\bar{p}' = 0.11$ at higher Strouhal numbers, to wit, $\Omega > 5$. However, for $\bar{p}' = 0.11$ and $\Omega < 5$ the signal is quite clean. Moreover, a clear dependence of the experimental results on $\bar{p}'$ is observed. E.g., one notes for $\bar{p}' = 0.11$ and 0.26—although the real part of the transfer impedance is very nearly identical— on the second hydrodynamic mode at $\Omega \simeq 2.5$ a significant deviation of ca. 14% in the inertial part $Z_{\mathrm{orf},I}/\Omega$. While for $\bar{p}' = 0.53$ the real and imaginary parts of the transfer impedance follow the global trends of the lower amplitude results, the highest amplitude $\bar{p}' = 2.63$ display drastically different behavior. Moreover, for $\bar{p}' = 2.63$ whistling potentiality is completely suppressed. At these high amplitudes the acoustic velocity amplitude within the orifice becomes comparable to the steady flow velocity. Acoustically induced back flow might occur.

We note that that LNSE model prediction (thin solid line in Fig. 10) deviates structurally from the empirical data. E.g., the Strouhal number prediction for the second hydrodynamic mode deviates by ca. −17%.

The experimental results for a rounded inlet, $R_{\mathrm{ust}}/R_{\mathrm{orf}} = 2$, are compared to the compressible LNSE model predictions (thin solid line) in Fig. 11. The thick dotted, thick dashed-dotted, thick dashed, and thick solid line are for $\bar{p}' = 0.11, 0.26, 0.53$ and 2.63, respectively. One sees that $Z_{\mathrm{orf},R}$ for $\bar{p}' = 0.11$ and $\Omega > 5$ is dominated by noise. It is interesting to note that for $\bar{Z}_{\mathrm{orf},R}$ is basically amplitude independent. A difference in $\bar{Z}_{\mathrm{orf},I}$ for $0.5 < \Omega < 3$ is observed between $\bar{p}' = 2.63$ and the lower forcing amplitudes. One notes, that the LNSE model predictions for $\bar{Z}_{\mathrm{orf},I}/\Omega$ differ wildly from the experimental results. That said, one observes that both the LNSE model and the measurements for all four $\bar{p}'$ show a completely suppressed whistling potentiality for $R_{\mathrm{ust}}/R_{\mathrm{orf}} = 2$.

Experimental results for the rounded-outlet orifice are shown in Fig. 12 for $\bar{p}' = 0.11$ (thick dotted line), 0.26 (dashed dotted line), 0.53 (thick dashed line), 2.63 (thick solid line). The results obtained with $\bar{p}' = 0.11$ for $\Omega > 5$ are dominated by noise. It is interesting to note that the highest forcing amplitude suppresses the orifice's whistling potentiality. Although quantitative agreement between the empirical data and the LNSE model is observed, obvious quantitative differences are discernible in e.g. the prediction of Ω for the first hydrodynamic mode.

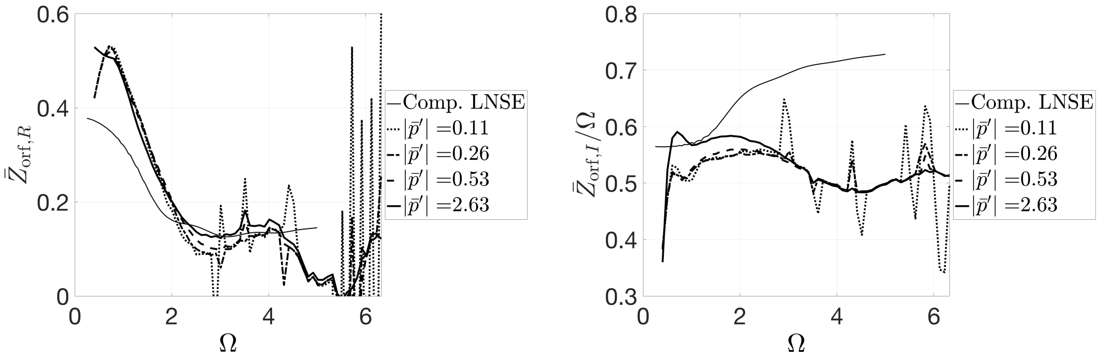

(a)

(b)

Fig. 11 Rounded-inlet sharp-edged outlet orifice, $R_{\mathrm{ust}}/R_{\mathrm{orf}} = 2$, measurements compared to compressible LNSE results: (a) $\bar{Z}_R$ vs. Ω (b) $\bar{Z}_I/\Omega$ vs. Ω.

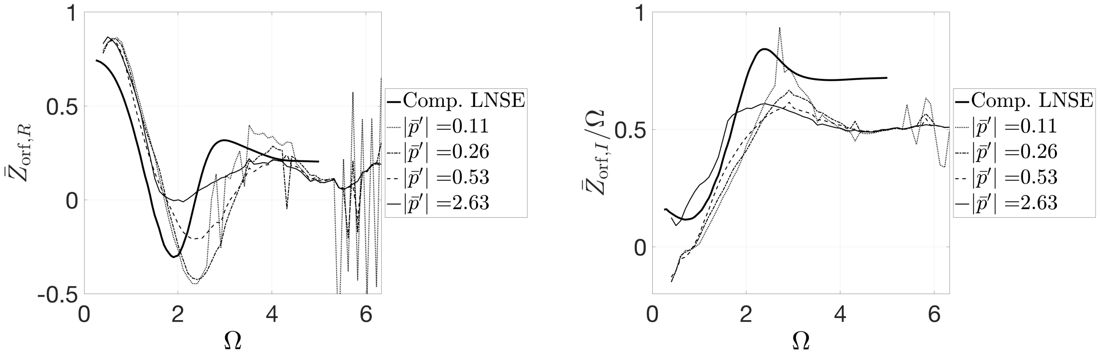

(a)

(b)

Fig. 12 Sharp-edged inlet rounded-outlet orifice, $R_{\mathrm{dst}}/R_{\mathrm{orf}} = 2$, measurements compared to compressible LNSE results: (a) $\bar{Z}_R$ vs. Ω (b) $\bar{Z}_I/\Omega$ vs. Ω.

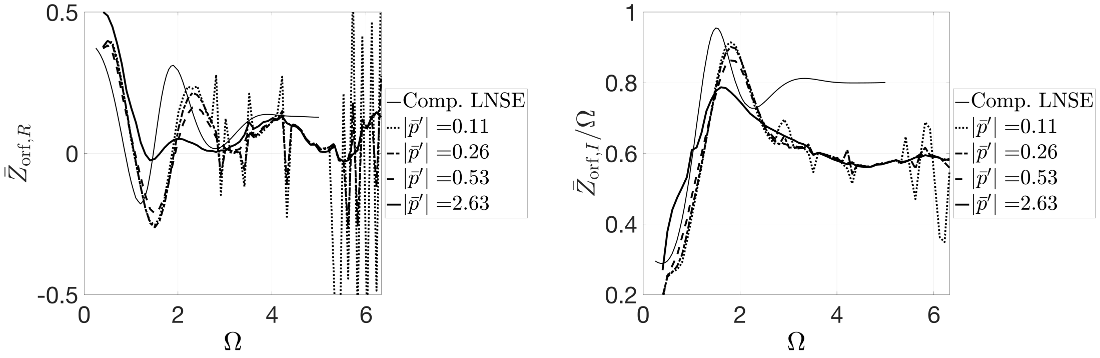

(a)

(b)

Fig. 13 Convergent-divergent nozzle orifice, $\theta_{\mathrm{dif}} = 0.52$ rad, measurements compared to compressible LNSE results: (a) $\bar{Z}_R$ vs. Ω (b) $\bar{Z}_I/\Omega$ vs. Ω.

Experimental and LNSE model results for the convergent-divergent nozzle orifice are shown in Fig. 13. Experimental data for $\bar{p}' = 0.11$ (thick dotted line), 0.26 (thick dashed dotted line), 0.53 (thick dashed line) and 2.63 (thick solid line) are shown. One noted that the signal for $\bar{p}' = 0.11$ with a Strouhal number above 5 is dominated by noise. That said, the experimental results for $\bar{p}' = 0.11$ and 0.26 are discerned to be essentially the same. This indicates that the results are in the linear regime. Notably, the whistling potentiality of the orifice appears to be suppressed for the highest forcing amplitude $\bar{p}' = 2.63$. In spite of the fact that qualitative agreement between the empirical data and the LNSE model is observed, clear quantitative differences are discernible in e.g. the prediction of Ω for the first hydrodynamic mode.

V. Discussion

The influence of an orifice's shape on its transfer impedance and by extension its whistling potentiality, were investigated using a LNSE model and experimentally. Four cylindrical orifice shapes were considered: a sharp-edged (inlet and outlet) orifice, a rounded-inlet sharp-edged outlet orifice, a sharp-edged inlet rounded outlet orifice, and a convergent-divergent nozzle orifice. The thickness of the plate containing the orifice, L_{orf}, was twice the minimum radius, R_{orf} of the orifice; viz., $L_{\mathrm{orf}} = 2R_{\mathrm{orf}}$. The individually probed orifices were subject to a bias flow, which was fixed such that the Reynolds number based on the orifice neck diameter $2R_{\mathrm{orf}}$ was $Re_{\mathrm{orf}} = 1.2 \times 10^3$.

The experimental and simulation results for sharp-edged orifice confirm that the second hydrodynamic mode—viz., the second and most pronounced local minimum in the real part of the transfer impedance of the orifice—has the largest whistling potentiality. This is in agreement with the experimental observations of Testud et al. [15] and Moers et al. [19]. The fact that they have a higher whistling potentiality than the first mode is due to the fact that at low Strouhal numbers the amplification of the perturbations by the shear layer perturbations increases exponentially with the ratio of shear layer length to hydrodynamic wavelength. Hence, the second hydrodynamic mode corresponds to an amplification of perturbations, which is the square of the amplification for the first mode. The fact that the third mode does not have a much larger whistling potentiality is due to the reduction of the amplification at higher Strouhal numbers. As predicted by Michalke [43], there is a critical Strouhal number based on the shear layer thickness above which the shear layer is hydrodynamically stable. This effect is therefore Reynolds dependent, as illustrated by the results presented by Fabre et al. [4] for the same orifice geometry. An interesting result obtained by Fabre et al. [4] is that the Strouhal number of the hydrodynamic modes is only weakly dependent on the Reynolds number and that when the plate thickness is used as reference length instead of R_{orf} the Strouhal number becomes almost independent of the plate thickness. A systematic study of the Reynolds number and plate thickness on the Strouhal number for the first two hydrodynamic modes is provided by Testud et al. [15]

In the case of the rounded-inlet sharp-outlet orifice, the results show that even for minor rounding $R_{\mathrm{ust}}/R_{\mathrm{orf}} = 1/40$ the whistling potentiality —i.e., compared to for $R_{\mathrm{ust}}/R_{\mathrm{orf}} > 1/10$ the whistling potentiality is essentially suppressed. These findings confirm and extend those found by Guzman-Iñigo et al. [5].

Results for the sharp-inlet rounded outlet orifice show that rounding of the outlet affects the whistling potentiality of the orifice significantly. Indeed, for $R_{\mathrm{dst}}/R_{\mathrm{orf}} > 4/10$ the orifice's whistling potentiality is shifted to the first hydrodynamic mode. I.e., rounding the downstream edge, whilst keeping the upstream edge sharp, enhances the whistling potentiality of the first hydrodynamic mode—yet reduces that of higher modes. It is noteworthy that Vortex Sound Theory qualitatively predicts this. Moreover, this confirms that the notion that sound production can only occur through impingement on e.g. a sharp-downstream edge is inadequate.

In the case of the convergent-divergent nozzle geometry, the first hydrodynamic mode was found to dominate its whistling potentiality. Moreover, the difussor angle, θ_{dif}, was varied systematically whilst keeping all other parameters of the problem fixed. For $\theta_{\mathrm{dif}} = 0.52$ an optimum in whistling potentiality was found. I.e., a orifice's shape can be changed to optimize its whistling potentiality. For diffusers (conical pipe diameter expansion) in gas transport systems, van Lier et al. [35] also found a large whistling potentiality at an angle of this magnitude.

In the experiments, the forcing-amplitude, $|\bar{p}'|$, was varied. Overall, one observes a dependence of the results on the amplitude for $\bar{p}' > 0.26$. I.e, results obtained with $\bar{p}' > 0.26$ are in the nonlinear regime.

Obviously, the nonlinear regime is formally outside of the LNSE model's application regime. That said, generally remarkable qualitative agreement is observed between the LNSE and experimental data. Notably, in some instances this qualitative agreement extends to experimental data in the nonlinear regime.

However, a structural quantitative deviation between the LNSE predictions and experimental data in the linear regime is noted. E.g., in the case of a sharp-edged orifice—even though $\bar{Z}_{\mathrm{orf},R_{\min}}$ is well predicted for the second hydrodynamic mode, viz., within a few percent—the corresponding Strouhal number deviates by ca. 17%. Moreover, the observed imaginary part was at high Strouhal numbers systematically lower than the predicted values.

Interestingly, the highest forcing amplitude, $\bar{p}' = 2.63$, was observed to suppress whistling potentiality. This can obviously not be predicted with a LNSE model.

VI. Conclusions

The shape of an orifice subject to a bias flow can significantly affect its transfer impedance and ergo its whistling potentiality. Moreover, an orifice's geometric parameters can be manipulated to optimize its whistling potentiality. It was experimentally observed that high forcing amplitudes suppress whistling potentiality. While the real part of the impedance (resistance) is not affected by the confinement of the orifice within a pipe, the imaginary part (inertance) is.

A. Flow controller calibration

The flow controller (Bronkhorst F202Av) used to set the volume flow was calibrated against a static pressure difference measurement at the highest available flow rate for the orifice with upstream rounded edge $R_{\text{ust}} = 2R_{\text{orf}}$ (without any acoustic forcing). These measurements were corrected for the influence of the displacement thickness of the viscous boundary layers. For moderately high Reynolds numbers $Re_{\text{orf}} = 9 \times 10^3$ as used for this calibration the boundary are laminar and rather thin compared to R_{orf}.

Using the method of Thwaites, one can determine the square of the momentum thickness

$$\delta_2^2 = \frac{0.45\nu}{U^6} \int_0^{L_{\text{orf}}} U^5 \mathrm{d}x \tag{26}$$

where x is the axial coordinate. Moreover, one has that

$$\delta_1 = H_{12}(L_{\text{orf}})\delta_2 \tag{27}$$

where $H_{12}(L_{\text{orf}}) = 2.61$ for $(\mathrm{d}U/\mathrm{d}x)_{x=L_{\text{orf}}} = 0$, as prevails at the exit of this orifice.

Assuming a quasi-1D flow across the rounded-inlet orifice (Fig. 2(b)) and neglecting the displacement thickness δ_1, one finds for the axial velocity

$$U = \left(\frac{R_{\text{orf}}}{R}\right)^2 U_{\text{orf}} \tag{28}$$

where

$$R = R_{\text{orf}} + L_{\text{orf}} - \sqrt{L_{\text{orf}}^2 - (L_{\text{orf}} - x)^2} \tag{29}$$

Eq. (26) can now be rewritten to find

$$\delta_2^2 = \frac{0.45\nu}{U_{\text{orf}}} R_{\text{orf}} \int_0^{L_{\text{orf}}/\mathrm{R}_{\text{orf}}} \left(\frac{R_{\text{orf}}}{R}\right)^{10} \mathrm{d}\left(\frac{x}{R_{\text{orf}}}\right) \tag{30}$$

We defined the integral

$$I \equiv \int_0^{L_{\text{orf}}/\mathrm{R}_{\text{orf}}} \left(\frac{R_{\text{orf}}}{R}\right)^{10} \mathrm{d}\left(\frac{x}{R_{\text{orf}}}\right) \tag{31}$$

which using Mathematica was found to be $I = 0.57$. Using Eq. (27), one finds

$$\frac{\delta_1}{R_{\text{orf}}} = H_{12}\left(L_{\text{orf}}\right) \sqrt{\left(\frac{2 \times 0.45}{Re_{\text{orf}}} I\right)} \tag{32}$$

We define

$$\alpha_{\text{tws}} = 1 - \frac{2\delta_1}{R_{\text{orf}}} \tag{33}$$

and note that

$$U_{\mathrm{orf}} = \alpha_{tws} U_{\max} \tag{34}$$

where $U_{\max}$ is the maximum velocity on the center line at the rounded inlet orifice's outlet. Using Bernoulli one finds

$$U_{\max} = \sqrt{\frac{2\Delta p}{\rho}} \tag{35}$$

The static pressure difference, Δp, measured by means of a TROTEC TA400 manometer (Fig. 4) across the rounded-inlet orifice (Fig. 2(b)) can now be related to the volumetric flow through it:

$$\dot{Q}_{\mathrm{msr}} = \pi R_{\mathrm{orf}}^2 \alpha_{\mathrm{tws}} U_{\max} = \pi R_{\mathrm{orf}}^2 \alpha_{\mathrm{tws}} \sqrt{\frac{2\Delta p}{\rho}} \tag{36}$$

Using the interface with the flow controller a volumetric flow, $\dot{Q}_{\mathrm{set}}$, can be set. $\dot{Q}_{\mathrm{set}} = 1.31 \times 10^{-3}\ \mathrm{m}^3 \cdot \mathrm{s}^{-1}$ was set (90% of the highest imposable volumetric-flow rate) and the corresponding $\Delta p = 119$ Pa was determined (uncertainty 1 Pa). One finds $U_{\mathrm{orf}} \simeq \alpha_{\mathrm{tws}} U_{\max} = 13.3\ \mathrm{m} \cdot \mathrm{s}^{-1}$, which yields $Re_{\mathrm{orf}} = 2R_{\mathrm{orf}} U_{\mathrm{orf}}/\nu = 8.87 \times 10^3$. Using Eqs. (32) and (36), one can determine $\alpha_{\mathrm{tws}} = 0.960$ and the calibration coefficient:

$$\frac{\dot{Q}_{\mathrm{msr}}}{\dot{Q}_{\mathrm{set}}} = 0.81 \tag{37}$$

Acknowledgements

The authors gratefully acknowledge the European Research Council (ERC)—who supported this work through the Consolidator Grant AFIRMATIVE (2018-2023). Alessia Aulitto received support and training through the Marie Skłodowska-Curie Initial Training Network Pollution Know-How and Abatement (POLKA)—as such, we are thankful for the financial support from the European Commission under call H2020-MSCA-ITN-2018 (project number: 813367). Thanks is due to Ines Lopez Arteaga. Lionel Hirschberg thanks Catherine Lemaitre and Assa Ashuach for their help.

References

[1] Zhao, D., and Li, X., "A review of acoustic dampers applied to combustion chambers in aerospace industry," *Progress in Aerospace Sciences*, Vol. 74, 2015, pp. 114–130. doi:https://doi.org/10.1016/j.paerosci.2014.12.003.

[2] Lahiri, C., and Bake, F., "A review of bias flow liners for acoustic damping in gas turbine combustors," *Journal of Sound and Vibration*, Vol. 400, 2017, pp. 564–605. doi:10.1016/j.jsv.2017.04.005.

[3] Fabre, D., Longobardi, R., Bonnefis, P., and Luchini, P., "The acoustic impedance of a laminar viscous jet through a thin circular aperture," *Journal of Fluid Mechanics*, Vol. 864, 2019, p. 5–44. doi:10.1017/jfm.2018.1008.

[4] Fabre, D., Longobardi, R., Citro, V., and Luchini, P., "Acoustic impedance and hydrodynamic instability of the flow through a circular aperture in a thick plate," *Journal of Fluid Mechanics*, Vol. 885, 2020, p. A11. doi:10.1017/jfm.2019.953.

[5] Guzmán-Iñigo, J., Yang, D., Johnson, H. G., and Morgans, A. S., "Sensitivity of the Acoustics of Short Circular Holes with Bias Flow to Inlet Edge Geometries," *AIAA Journal*, Vol. 57, No. 11, 2019, pp. 4835–4844. doi:10.2514/1.J057996.

[6] Sondhauss, C. F. J., "Über die Beim Ausströmen der Luft Entstehende Töne," *Pogg. Ann. Phys. Chem.*, Vol. 91, 1854, pp. 126–147.

[7] Rayleigh, L., *Theory of Sound*, Vol. 2, Dover Publications, Inc., New York, 1945.

[8] Anderson, A. B. C., "Dependence of Pfeifenton (Pipe Tone) Frequency on Pipe Length, Orifice Diameter, and Gas Discharge Pressure," *The Journal of the Acoustical Society of America*, Vol. 24, No. 6, 1952, pp. 675–681. doi:10.1121/1.1906955.

[9] Anderson, A. B. C., "A Circular-Orifice Number Describing Dependency of Primary Pfeifenton Frequency on Differential Pressure, Gas Density, and Orifice Geometry," *The Journal of the Acoustical Society of America*, Vol. 25, No. 4, 1953, pp. 626–631. doi:10.1121/1.1907154.

[10] Anderson, A. B. C., "A Jet-Tone Orifice Number for Orifices of Small Thickness-Diameter Ratio," *The Journal of the Acoustical Society of America*, Vol. 26, No. 1, 1954, pp. 21–25. doi:10.1121/1.1907284.

[11] Anderson, A. B. C., "Structure and Velocity of the Periodic Vortex-Ring Flow Pattern of a Primary Pfeifenton (Pipe Tone) Jet," *The Journal of the Acoustical Society of America*, Vol. 27, No. 6, 1955, pp. 1048–1053. doi:10.1121/1.1908112.

[12] Anderson, A. B. C., "Vortex-Ring Structure-Transition in a Jet Emitting Discrete Acoustic Frequencies," *The Journal of the Acoustical Society of America*, Vol. 28, No. 5, 1956, pp. 914–921. doi:10.1121/1.1908516.

[13] Jing, X., and Sun, X., "Effect of plate thickness on impedance of perforated plates with bias flow," *AIAA journal*, Vol. 38, 2000, pp. 1573–1578.

[14] Karthik, B., R., C. S., and I., S. R., "Mechanism of pipe-tone excitation by flow through an orifice in a duct," *Int. J. Aeroacoustics*, Vol. 7, No. 3-4, 2008, pp. 321–348. doi:10.1260/1475-472X.7.3.321.

[15] Testud, P., Aurégan, Y., Moussou, P., and Hirschberg, A., "The whistling potentiality of an orifice in a confined flow using an energetic criterion," *Journal of Sound and Vibration*, Vol. 325, No. 4, 2009, pp. 769–780. doi:https://doi.org/10.1016/j.jsv.2009.03.046.

[16] Lacombe, R., Moussou, P., and Aurégan, Y., "Whistling of an orifice in a reverberating duct at low Mach number," *The Journal of the Acoustical Society of America*, Vol. 130, No. 5, 2011, pp. 2662–2672. doi:10.1121/1.3641427.

[17] Zhou, L., and Bodén, H., "Experimental investigation of an in-duct orifice with bias flow under medium and high level acoustic excitation," *International Journal of Spray and Combustion Dynamics*, Vol. 6, 2014, pp. 267–292.

[18] Su, J., Rupp, J., Garmory, A., and Carrotte, J., "Measurements and computational fluid dynamics predictions of the acoustic impedance of orifices," *Journal of Sound and Vibration*, Vol. 352, 2015, pp. 174–191.

[19] Moers, E., Tonon, D., and Hirschberg, A., "Strouhal number dependency of the aero-acoustic response of wall perforations under combined grazing-bias flow," *Journal of Sound and Vibration*, Vol. 389, 2017, pp. 292–308. doi:https://doi.org/10.1016/j.jsv.2016.11.028.

[20] Wu, G., Guan, Y. H., Ji, C., and Gay, F. Y. X., "Experimental studies on sound absorption coefficients of perforated pipes with bias-grazing flows at low Mach and Strouhal number," *Aerospace Science and Technology*, Vol. 107, 2020, p. 106255. doi:10.1016/j.ast.2020.106255.

[21] Nair, V., and Sujith, R., "Precursors to self-sustained oscillations in aeroacoustic systems," *International Journal of Aeroacoustics*, Vol. 15, No. 3, 2016, pp. 312–323. doi:10.1177/1475472X16630877.

[22] Moussou, P., "Acoustically Induced Instabilities in Pipes by the Nyquist Criterion," *Proceedings of ASME 2014 Pressure Vessels & Piping Division Conference*, Pressure Vessels and Piping Conference, Vol. 4: Fluid-Structure Interaction, 2014, pp. 1–9. doi:10.1115/PVP2014-28306.

[23] Kopitz, J., and Polifke, W., "CFD-based application of the Nyquist criterion to thermo-acoustic instabilities," *Journal of Computational Physics*, Vol. 227, 2008, p. 6754–6778. doi:10.1016/j.jcp.2008.03.022.

[24] Ji, C., and Zhao, D., "Lattice Boltzmann investigation of acoustic damping mechanism and performance of an in-duct circular orifice," *The Journal of the Acoustical Society of America*, Vol. 135, 2014, p. 3243–3251. doi:10.1121/1.4876376.

[25] Chen, Z., Ji, Z., and Huang, H., "Acoustic impedance of perforated plates in the presence of bias flow," *Journal of Sound and Vibration*, Vol. 446, 2019, pp. 159–175. doi:10.1016/j.jsv.2019.01.031.

[26] Alenius, E., Åbom, M., and Fuchs, L., "Large eddy simulations of acoustic-flow interaction at an orifice plate," *Journal of Sound and Vibration*, Vol. 345, 2015, pp. 162–177. doi:https://doi.org/10.1016/j.jsv.2015.02.012.

[27] Alenius, E., "Mode switching in a thick orifice jet, an LES and dynamic mode decomposition approach," *Computers & Fluids*, Vol. 90, 2014, pp. 101–112. doi:https://doi.org/10.1016/j.compfluid.2013.11.022.

[28] Sovardi, C., Jaensch, S., and Polifke, W., "Concurrent identification of aero-acoustic scattering and noise sources at a flow duct singularity in low Mach number flow," *Journal of Sound and Vibration*, Vol. 377, 2016, pp. 90–105. doi:https://doi.org/10.1016/j.jsv.2016.05.025.

[29] Kierkegaard, A., Boij, S., and Efraimsson, G., "A frequency domain linearized Navier–Stokes equations approach to acoustic propagation in flow ducts with sharp edges," *The Journal of the Acoustical Society of America*, Vol. 127, No. 2, 2010, pp. 710–719. doi:10.1121/1.3273899.

[30] Kierkegaard, A., Allam, S., Efraimsson, G., and Åbom, M., "Simulations of whistling and the whistling potentiality of an in-duct orifice with linear aeroacoustics," *Journal of Sound and Vibration*, Vol. 331, No. 5, 2012, pp. 1084–1096. doi:https://doi.org/10.1016/j.jsv.2011.10.028.

[31] Tonon, D., Moers, E., and Hirschberg, A., "Quasi-steady acoustic response of wall perforations subject to a grazing-bias flow combination," *Journal of Sound and Vibration*, Vol. 332, No. 7, 2013, pp. 1654–1673. doi:https://doi.org/10.1016/j.jsv.2012.11.024.

[32] Temiz, M. A., Lopez Arteaga, I., Efraimsson, G., Åbom, M., and Hirschberg, A., "The influence of edge geometry on end-correction coefficients in micro perforated plates," *The Journal of the Acoustical Society of America*, Vol. 138, No. 6, 2015, pp. 3668–3677. doi:10.1121/1.4937748.

[33] Howe, M. S., *Acoustics of fluid-structure interactions*, Cambridge university press, Cambridge, UK, 1998. doi:10.1017/CBO9780511662898.

[34] Hirschberg, A., Bruggeman, J.C., A., Wijnands, and Smits, N., "The whistler nozzle and horn as aeroacoustics sound source in pipe systems," *Acta Acustica United with Acoustica*, Vol. 68, No. 2, 1989, p. 157–160.

[35] van Lier, L., Dequand, S., Hirschberg, A., and Gorter, J., "Aeroacoustics of diffusers: An experimental study of typical industrial diffusers at Reynolds numbers of 10^5," *The Journal of the Acoustical Society of America*, Vol. 109, No. 1, 2001, pp. 108–115. doi:10.1121/1.1329618.

[36] Nakiboğlu, G., Manders, H. B. M., and Hirschberg, A., "Aeroacoustic power generated by a compact axisymmetric cavity: prediction of self-sustained oscillation and influence of the depth," *Journal of Fluid Mechanics*, Vol. 703, 2012, p. 163–191. doi:10.1017/jfm.2012.203.

[37] Guzmán-Iñigo, J., Yang, D., Gaudron, R., and Morgans, A. S., "On the scattering of entropy waves at sudden area expansions," *Manuscript under review*, 2021. URL `https://arxiv.org/abs/2111.13043`.

[38] Schaefer, K. L., Jones, T. D., Hill, R., Mella, H., Sim, S. J., and Yamamoto, K., "FEniCsx computing platform," `https://fenicsproject.org`, 2022.

[39] Matsumoto, J., and Kawahara, M., "Shape identification for fluid-structure interaction problem using improved bubble element," *International Journal of Computational Fluid Dynamics*, Vol. 15, No. 1, 2001, pp. 33–45.

[40] Aulitto, A., Hirschberg, A., Lopez Arteaga, I., and Buijssen, E., "Effect of slit length on linear and non-linear acoustic transfer impedance of a micro-slit plate," *Acta Acust.*, Vol. 6, No. 6, 2022. doi:10.1051/aacus/2021059.

[41] Jang, S.-H., and Ih, J.-G., "On the multiple microphone method for measuring in-duct acoustic properties in the presence of mean flow," *The Journal of the Acoustical Society of America*, Vol. 103, No. 3, 1998, pp. 1520–1526. doi:10.1121/1.421289.

[42] Naderyan, V., Raspet, R., Hickey, C. J., and Mohammadi, M., "Acoustic end corrections for micro-perforated plates," *The Journal of the Acoustical Society of America*, Vol. 146, No. 4, 2019, pp. EL399–EL404. doi:10.1121/1.5129560.

[43] Michalke, A., "On spatially growing disturbances in an inviscid shear layer," *Journal of Fluid Mechanics*, Vol. 23, No. 3, 1965, p. 521–544. doi:10.1017/S0022112065001520.